Sub-MeV Electron Precipitation Driven by EMIC Waves through Nonlinear Fractional Resonances

M. Hanzelka[1,2], W. Li[1], M. Qin[1], L. Capannolo[1], X. Shen[1], Q. Ma[1,3], L. Gan[1], V. Angelopoulos[4]

[1]Center for Space Physics, Boston University, Boston, MA, USA
[2]Department of Space Physics, Institute of Atmospheric Physics of the Czech Academy of Sciences, Prague, Czech Republic
[3]Department of Atmospheric and Oceanic Sciences, UCLA, Los Angeles, CA, USA
[4]Earth, Planetary, and Space Sciences Department, and Institute of Geophysics and Planetary Physics, UCLA, Los Angeles, CA, USA

Key Points:

- Electrons resonate with intense quasiparallel EMIC waves at fractions of the minimum resonance energy
- Fractional resonant scattering causes significant precipitation when the wave amplitude reaches above 1% of the ambient field
- Precipitating electron flux spectrum observed by the ELFIN CubeSats supports the estimated influence of fractional resonances

Corresponding author: Miroslav Hanzelka, `mirekhanzelka@gmail.com`

Abstract

Electromagnetic ion cyclotron waves in the Earth's outer radiation belt drive rapid electron losses through wave-particle interactions. The precipitating electron flux can be high in the 100s keV energy range, well below the typical minimum resonance energy. One of the proposed explanations relies on nonresonant scattering, which causes pitch-angle diffusion away from the fundamental cyclotron resonance. Here we propose the fractional sub-cyclotron resonance, a second-order nonlinear effect that scatters particles at resonance order $n = 1/2$, as an alternate explanation. Using test-particle simulations, we evaluate the precipitation ratios of sub-MeV electrons for wave packets with various shapes, amplitudes, and wave normal angles. We show that the nonlinear sub-cyclotron scattering produces larger ratios than the nonresonant scattering when the wave amplitude reaches sufficiently large values. The ELFIN CubeSats detected several events with precipitation ratio patterns matching our simulation, demonstrating the importance of sub-cyclotron resonances during intense precipitation events.

Plain Language Summary

High-energy electrons in the Earth's radiation belt are constantly being scattered by the ubiquitous electromagnetic plasma waves. A portion of these scattered electrons is lost to the atmosphere, where the particles deposit their energy and cause a chain of chemical reactions possibly contributing to ozone destruction. The energy and flux of the precipitating electrons depend on the nature of the wave-particle interactions in the radiation belt. The electromagnetic ion cyclotron wave (EMIC), known to be responsible for scattering relativistic electrons, has been observed to cause precipitation at energies much lower than expected by the standard theory. We numerically investigate two types of interactions, the nonresonant scattering and the nonlinear sub-cyclotron scattering, and show how both influence the relative precipitating fluxes. We demonstrate that sub-cyclotron interactions driven by intense EMIC waves can cause stronger precipitation than nonresonant scattering at sub-MeV energies. The dual ELFIN CubeSats detected precipitation profiles that match our numerical results, confirming the importance of nonlinear sub-cyclotron scattering in the analysis of intense precipitation events.

1 Introduction

The Earth's outer radiation belt is sustained by a dynamic balance between particle injections, acceleration, transport, and losses (Shprits et al., 2008; Reeves et al., 2013; Baker et al., 2019; Li & Hudson, 2019). One major particle loss driver is the electromagnetic ion cyclotron (EMIC) waves, which interact with energetic protons and relativistic electrons (Jordanova et al., 2001; Usanova et al., 2014; Zhu et al., 2020; Lyu et al., 2022). The EMIC waves are located predominantly near the equatorial plane (Allen et al., 2015), propagating quasiparallel to the local magnetic field line (Min et al., 2012). During geomagnetically active times, intense EMIC waves occur in the noon-to-dusk sector at radial distances from 4 to 6.5 Earth's radii (Saikin et al., 2016; Zhang et al., 2016), causing rapid pitch-angle scattering of high-energy radiation belt electrons through cyclotron resonance (Horne & Thorne, 1998). The lost electrons deposit their energy in the upper atmosphere, contributing to changes in atmospheric chemistry (Thorne, 1977; Seppälä et al., 2015).

The minimum cyclotron resonance energy of electrons interacting with EMIC waves is given by the approximate formula (Chen et al., 2019)

$$E_{\mathrm{Rmin}} \approx mc^2 \left(\sqrt{1 + \frac{n^2 \Omega_{\mathrm{e}}^2}{k_\parallel^2 c^2}} - 1 \right) . \tag{1}$$

Here m stands for the electron mass, c is the speed of light, Ω_{e} is the local electron gyrofrequency, $k_\parallel$ is the parallel wavenumber, and n represents the resonance order. For quasiparallel waves, the fundamental resonance $n = 1$ dominates. Electrons with pitch angle $\alpha = 0°$ and kinetic energy $E_{\mathrm{k}} = E_{\mathrm{Rmin}}$ resonate with EMIC waves when propagating along the wave field. With oblique waves, strong resonance is possible in both directions (Wang et al., 2017; Hanzelka, Li, & Ma, 2023). The resonance energy increases with pitch angle, following the resonance curves (Summers et al., 1998). For the typical EMIC wave parameters, E_{Rmin} stays above 1 MeV (Miyoshi et al., 2008; Meredith et al., 2014). However, recent studies show growing evidence of EMIC waves causing significant precipitating electron fluxes down to hundreds of keV (Ukhorskiy et al., 2010; Clilverd et al., 2015; Hendry et al., 2019; Denton et al., 2019; Capannolo et al., 2021, 2023a). According to Equation 1, sub-MeV energies can be reached by the fundamental resonance when $k_\parallel$ is sufficiently high — this is possible when the electron plasma-to-gyrofrequency ratio ($\omega_{\mathrm{pe}}/\Omega_{\mathrm{e}}$) is large or when the wave frequency gets close to local ion gyrofrequencies (Li et al., 2007; Min et al., 2022). Sub-MeV electrons can also interact with EMIC waves through nonresonant scattering, a type of interaction associated with wave packet modulations (Chen et al., 2016). The nonresonant interaction is tied to the fundamental resonance but can extend efficient pitch-angle diffusion down to hundreds of keV when the wave field consists of very short packets (An et al., 2022).

Here we propose that nonlinear effects can contribute to sub-MeV electron precipitation through resonant scattering at the $n = 1/2$ fraction of gyrofrequency. This type of resonance was studied by Fu et al. (2015) in the case of whistler-mode waves and, more recently, by Hanzelka, Li, and Ma (2023) within the frame of the electron-EMIC interactions. Assuming a fundamental resonance energy of $\sim 1\,\mathrm{MeV}$, the $n = 1/2$ resonance affects electrons at around $400\,\mathrm{keV}$, making it a plausible explanation for sub-MeV precipitation. Hanzelka, Li, and Ma (2023) numerically demonstrated that the $n = 1/2$ resonance appears only during oblique propagation (wave normal angle $\theta_{\mathrm{k}} > 0$). They also provided a simplified analytical derivation indicating that the standard deviation in energy and pitch angle grows with the second power of wave amplitude, B_{w}^2, unlike the $n = 1$ resonance, which scales with the first power (where B_{w} is the wave magnetic field amplitude). Therefore, this fractional resonance is expected to be efficient only during high-amplitude events.

To evaluate nonresonant and nonlinear sub-cyclotron scattering of electrons in the $E_{\mathrm{k}} < 1\,\mathrm{MeV}$ range, we perform test-particle simulations using EMIC wave models with various packet shapes, amplitudes, and wave normal angles (WNA). In Section 2.1, we describe our numerical method and input parameters. Section 2.2 briefly describes the dataset of ELFIN CubeSats particle measurements. In Section 3, we present a parametric analysis of pitch-angle diffusion and precipitation fluxes and compare the results with selected events from ELFIN observations. In Section 4, we discuss and summarize our findings.

2 Methods

2.1 Test-particle Simulations

We employ the test-particle simulation method following Hanzelka, Li, and Ma (2023). The particles are evolved by the relativistic Boris algorithm with phase angle correction (Zenitani & Umeda, 2018). The integration time step adapts to the background magnetic field, sampling the local electron gyroperiod with 128 points. All simulations are performed in one spatial dimension along a dipole field line $L = 6$ with background magnetic field $B_0 = 143.5\,\mathrm{nT}$ at the equatorial minimum. The ratio of equatorial plasma frequency to gyrofrequency is set to $\omega_{\mathrm{pe0}}/\Omega_{\mathrm{e0}} = 15$, and the relative concentrations of protons, He+ ions, and O+ ions are in a ratio of $90 : 5 : 5$.

The wave model assumes hydrogen band EMIC waves with a constant frequency $\omega = 0.66\Omega_{\mathrm{p0}}$, where Ω_{p0} is the equatorial proton gyrofrequency. Solving the cold plasma dispersion relation with wave normal angle $\theta_{\mathrm{k}} = 0°$ gives us wavelength $\lambda_{\mathrm{w}} \approx 210\,\mathrm{km}$, and plugging the corresponding wavenumber into Equation 1 results in minimum resonance energy $E_{\mathrm{Rmin}} \approx 1.0\,\mathrm{MeV}$. Three amplitude profiles are used: a single packet with a field-aligned length $h_{\mathrm{wp}} = 16\lambda_{\mathrm{w}}$, two packets each $h_{\mathrm{wp}}/2$ long, and four packets each $h_{\mathrm{wp}}/4$ long. Individual subpackets are modeled with $\cos^2(\pi h/(2d_{\mathrm{e}}))$, where d_{e} represents the half-width. The smallest value, $d_{\mathrm{e}} = 2\lambda_{\mathrm{w}}$, matches with the shortest subpackets reported by Chen et al. (2016) and An et al. (2022). Each wave profile can have four amplitude values, $B_{\mathrm{w0}} = \{0.005, 0.01, 0.02, 0.04\}B_0$, and three WNA values, $\theta_{\mathrm{k}} = \{0°, 15°, 30°\}$. The largest amplitude is comparable to the extremely strong EMIC waves reported by Engebretson et al. (2015), which peaked at $B_{\mathrm{w0}} \approx 0.06B_0$. Due to short simulation times, group velocity motion is not included.

To obtain the pitch angle diffusion coefficient, we launch particles from $h = 0$ and let them propagate to $h = 16\lambda_{\mathrm{w}}$ and record the pitch angle variations. The initial energies are sampled logarithmically from 0.3 MeV to 3 MeV with 96 points, the pitch angles are sampled uniformly from 0° to 45° with 45 points, and the gyrophases are sampled uniformly with $N_\varphi = 72$ points over the full angle. The changes in equatorial pitch angle α_{eq} are calculated for all particles in each energy–pitch-angle bin and combined into the diffusion coefficient

$$D_{\alpha\alpha} = \frac{1}{2\tau_{\mathrm{qb}}}\frac{1}{N_\varphi}\sum_{i=1}^{N_\varphi}\left(\alpha_{\mathrm{eq}i} - \frac{1}{N_\varphi}\sum_{j=1}^{N_\varphi}\alpha_{\mathrm{eq}j}\right)^2 , \qquad (2)$$

where τ_{qb} is the quarter-bounce period. As the propagation is quasiparallel, interactions during electron motion back toward the equator are not considered. For visualization of trajectories, pitch angle evolution is sampled with four points per gyroperiod.

The perturbations in phase space density are obtained from backward-in-time simulations with Liouville mapping (Hanzelka, Li, & Ma, 2023). The initial energetic electron distribution is a sum of five relativistic bi-Maxwellian distributions with parallel thermal velocities $U_{\mathrm{t}\parallel}/c = \{0.2, 0.5, 1.0, 2.5, 9.0\}$, perpendicular thermal velocities $U_{\mathrm{t}\perp}/c = \{0.3, 0.75, 1.5, 3.75, 14.5\}$, and relative hot plasma densities $n_{\mathrm{hot}}/n_{\mathrm{cold}} = \{0.05, 0.005, 5\cdot 10^{-4}, 5\cdot 10^{-5}, 5\cdot 10^{-9}\}$. As we seek relative changes in phase space density and EMIC waves affect the electron energy negligibly, the exact values of hot plasma density and thermal velocities are unimportant, leaving anisotropy $A = U_{\mathrm{t}\perp}^2/U_{\mathrm{t}\parallel}^2 - 1 = 1.25$ as the sole relevant parameter. The loss cone content of the perturbed PSD $f_{\mathrm{p}}(h_{\mathrm{wp}})$ at each energy level is divided by the PSD just outside the loss cone, resulting in the precipitation ratio

$$\frac{f_{\mathrm{in}}}{f_{\mathrm{out}}} = \frac{\int_{\alpha_{\mathrm{lc}}}^{\alpha_{\mathrm{sc90}}} \sin\alpha \,\mathrm{d}\alpha}{\int_{0}^{\alpha_{\mathrm{lc}}} \sin\alpha \,\mathrm{d}\alpha} \frac{\int_{0}^{\alpha_{\mathrm{lc}}} f_{\mathrm{p}} \sin\alpha \,\mathrm{d}\alpha}{\int_{\alpha_{\mathrm{lc}}}^{\alpha_{\mathrm{sc90}}} f_{\mathrm{p}} \sin\alpha \,\mathrm{d}\alpha}. \tag{3}$$

The loss cone angle α_{lc} is about 2.9° at the end of the wave packet, and α_{sc90} is the pitch angle of an electron at h_{wp} with a mirroring point at the altitude of the low Earth orbit (LEO) spacecraft. In other words, particles in the range $(\alpha_{\mathrm{lc}}, \alpha_{\mathrm{sc90}})$ constitute the population that would be observed as quasi-trapped by the spacecraft. For the purpose of PSD simulations, the pitch angles are sampled from 0° to 15° with 90 points.

2.2 ELFIN Spacecraft Flux Data

The dual ELFIN CubeSats (on a polar LEO at 300-450 km of altitude) provided electron flux data from July 2019 to September 2022. The energetic particle detector (EPDE) measured electrons over the range of 50 to 5000 keV sampled by 16 approximately logarithmic bins (Angelopoulos et al., 2020, 2023). The satellites had a spin period of ~ 3 seconds and twice per spin provided flux measurements nominally over the whole 180° range of pitch angles with 22.5° spin phase resolution, allowing for differentiation of particles inside and outside the local loss cone.

We utilize the dataset of 144 EMIC-driven precipitation events identified by Capannolo et al. (2023a) using precipitation signatures from proton measurements by NOAA POES when conjugate to ELFIN as a proxy for EMIC waves. Events with electron precipitation ratio decreasing with energy in the low hundreds of keV range are not part of this dataset, as such profiles indicate the presence of whistler waves (Ma et al., 2016; Angelopoulos et al., 2023). However, the coexistence of other waves with EMICs cannot be completely ruled out without direct observations; refer to Capannolo et al. (2023a) for details. Based on simulation results from Section 3, we visually selected 6 events that show patterns related to nonlinear fractional resonance. In the selection process, we sought precipitation profiles where a large precipitation ratio (> 0.75) is reached at energies below 1.5 MeV but above 0.7 MeV; that is, in a range of energies that can be affected by the fundamental cyclotron resonance under favorable conditions (see Equation 1 and the paragraph below it). The lowest energy bin with a ratio > 0.75 was labeled E_{k}^{*}. We then checked if a peak or plateau appeared near $E_{\mathrm{k}}^{*}/2$. Unlike in Capannolo et al. (2023a), we did not subtract backscattered electrons from the precipitating ones, and we used the full resolution half-spin data (one pitch-angle sweep per ~ 1.5 seconds) instead of the full-spin data. Time stamps for the selected events can be found in the Supporting Information, Table S1.

3 Results

In Figure 1, we show particle trajectories and diffusion coefficients $D_{\alpha\alpha}$ for three selected combinations of wave parameters. In the first case, we choose a long, unmodulated wave packet ($d_{\mathrm{e}} = 8\lambda_{\mathrm{w}}$) with a moderate amplitude ($B_{\mathrm{w0}}/B_0 = 1\%$) and $0°$ wave normal angle. The trajectories in Figure 1a show the equatorial pitch angle evolution of particles undergoing a combination of phase trapping and phase bunching, a typical behavior of electrons in resonance with large amplitude EMICs (Albert & Bortnik, 2009). This is an example of nonlinear effects driven by the fundamental cyclotron resonance. Figure 1b shows that the associated $D_{\alpha\alpha}$ drops to negligible values below 700 keV. The weakening of diffusion near $E_{\mathrm{k}} = 1\,\mathrm{MeV}$, $\alpha_{\mathrm{eq}} = 0°$, is caused by anomalous scattering, an advective process affecting low-α resonant electrons (Bortnik et al., 2022; Hanzelka, Li, & Ma, 2023).

Figures 1c and 1d demonstrate diffusive behavior in an extremely strong ($B_{\mathrm{w0}}/B_0 = 4\%$) parallel-propagating EMIC wave with short subpacket modulations ($d_{\mathrm{e}} = 2\lambda_{\mathrm{w}}$). The trajectories in Figure 1c show that after passing through a subpacket, the electrons spread out in pitch angle, even though their energy $E_{\mathrm{k}} = 0.594\,\mathrm{MeV}$ is far from $E_{\mathrm{Rmin}} \approx 1.0\,\mathrm{MeV}$. The pitch angle change depends not only on the amplitude gradient but also on the subpacket length, as electrons are released at different phases of their oscillatory motion (Chen et al., 2016). This is an example of nonresonant scattering. Diffusion coefficients in Figure 1d remain significant down to 300 keV, and high values of $> 0.1\,\mathrm{s}^{-1}$ are seen in a much wider range of energies than for long, weaker amplitude, unmodulated wave packets. The stripe structures in $D_{\alpha\alpha}$ arise due to the aforementioned phase dependence.

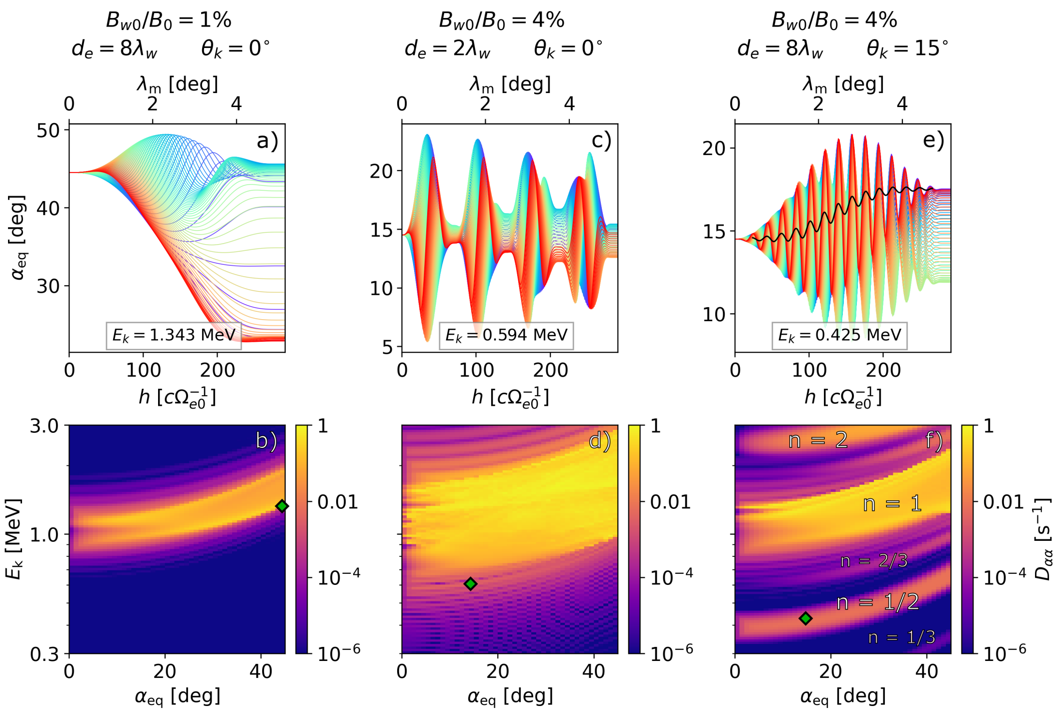

Figure 1. Selected examples of resonant and nonresonant interactions. a) Trajectories of electrons starting at pitch angle $\alpha_{eq} = 44.5°$ with energy $E_k = 1.343$ MeV, illustrating the phase trapping and bunching behavior near the fundamental cyclotron resonance $n = 1$. Line colors represent the uniformly sampled initial gyrophase φ, and λ_m is the magnetic latitude. b) Diffusion coefficient in energy–pitch-angle space. The green square shows the α_{eq}, E_k values used in the trajectory plot. c,d) Similar to panels a and b but with a higher wave amplitude and sub-packet modulations, demonstrating nonresonant scattering. e,f) Similar to panels a and b but the wave is strong and $\theta_k = 15°$. The trajectories demonstrate nonlinear sub-cyclotron scattering, with the black line showing a moving average of particle trajectory with initial gyrophase $\varphi = 0°$ (red line). Various resonance orders are labeled in the diffusion plot.

The last couple of panels, Figures 1e and 1f, retain the extremely high amplitude $B_{\mathrm{w}0}/B_0 = 4\%$, but the packet is long ($d_{\mathrm{e}} = 8\lambda_{\mathrm{w}}$), and the wave propagation direction is slightly oblique ($\theta_{\mathrm{k}} = 15°$). The trajectories in Figure 1e now exhibit large variations in pitch angle even at the low energy of 0.425 MeV. Examining a single trajectory, such as the red curve with $\varphi(h = 0) = 0°$, reveals that oscillations slowly grow and then fade again, excluding nonresonant scattering. The moving average of this trajectory (black line) reveals a slow drift toward higher pitch angles, while the combined effect on all trajectories is a symmetric spread in α_{eq}. This behavior is caused by the nonlinear resonance of fractional order $n = 1/2$. Figure 1f confirms the resonant nature of this diffusive behavior, with high $D_{\alpha\alpha}$ values localized along the $n = 1/2$ resonance curve, distinct from the nonresonant widening of the fundamental resonance. The diffusion plot also captures the $n = 2$ harmonic resonance and two minor fractional resonances with orders $n = 2/3$ and $n = 1/3$, which are of little significance for sub-MeV precipitation.

To visually represent diffusion coefficients for all 36 combinations of wave parameters, we plot them in Figure 2 as one-dimensional line plots for two selected initial pitch angles $\alpha_{\mathrm{eq}} = 2.5°$ and $\alpha_{\mathrm{eq}} = 14.5°$. The first value represents the bin closest to the loss cone; the second was chosen to limit the influence of anomalous scattering on $D_{\alpha\alpha}$. A 3-point moving average over energies was used to suppress the stripe structure related to nonresonant scattering that appeared in Figure 1d. Parallel propagation results in Figures 2a-d reveal that the resonance peak widens with amplitude. $D_{\alpha\alpha}$ at energies farther from the resonance increases by approximately an order of magnitude from $d_{\mathrm{e}} = 8\lambda_{\mathrm{w}}$ to $d_{\mathrm{e}} = 4\lambda_{\mathrm{w}}$, and another order of magnitude from $d_{\mathrm{e}} = 4\lambda_{\mathrm{w}}$ to $d_{\mathrm{e}} = 2\lambda_{\mathrm{w}}$. The $D_{\alpha\alpha}$ peak near $E_{\mathrm{k}} = 1\,\mathrm{MeV}$ grows with wave amplitude at $\alpha_{\mathrm{eq}} = 14.5°$, but this trend is less clear at the loss cone, where anomalous scattering effects are prominent.

The $D_{\alpha\alpha}$ peak associated with the $n = 1/2$ resonance appears near $E_{\mathrm{k}} = 400\,\mathrm{keV}$ when we increase the WNA to $\theta_{\mathrm{k}} = 15°$ (Figures 2e-h). For the unmodulated wave packet and with $\alpha_{\mathrm{eq}} = 14.5°$ (blue dashed line), the peak grows about 16 times with each doubling of wave amplitude, confirming the B_{w}^4 scaling expected for this fractional resonance. The model with short subpackets predicts a slightly lower $D_{\alpha\alpha}$ than the single long packet but widens the resonance peak. Consequently, the modulated packet can cause a nearly constant diffusion rate between 300 and 700 keV (Figure 2h). This result of combined nonresonant and nonlinear scattering predicts vastly different diffusion rates compared

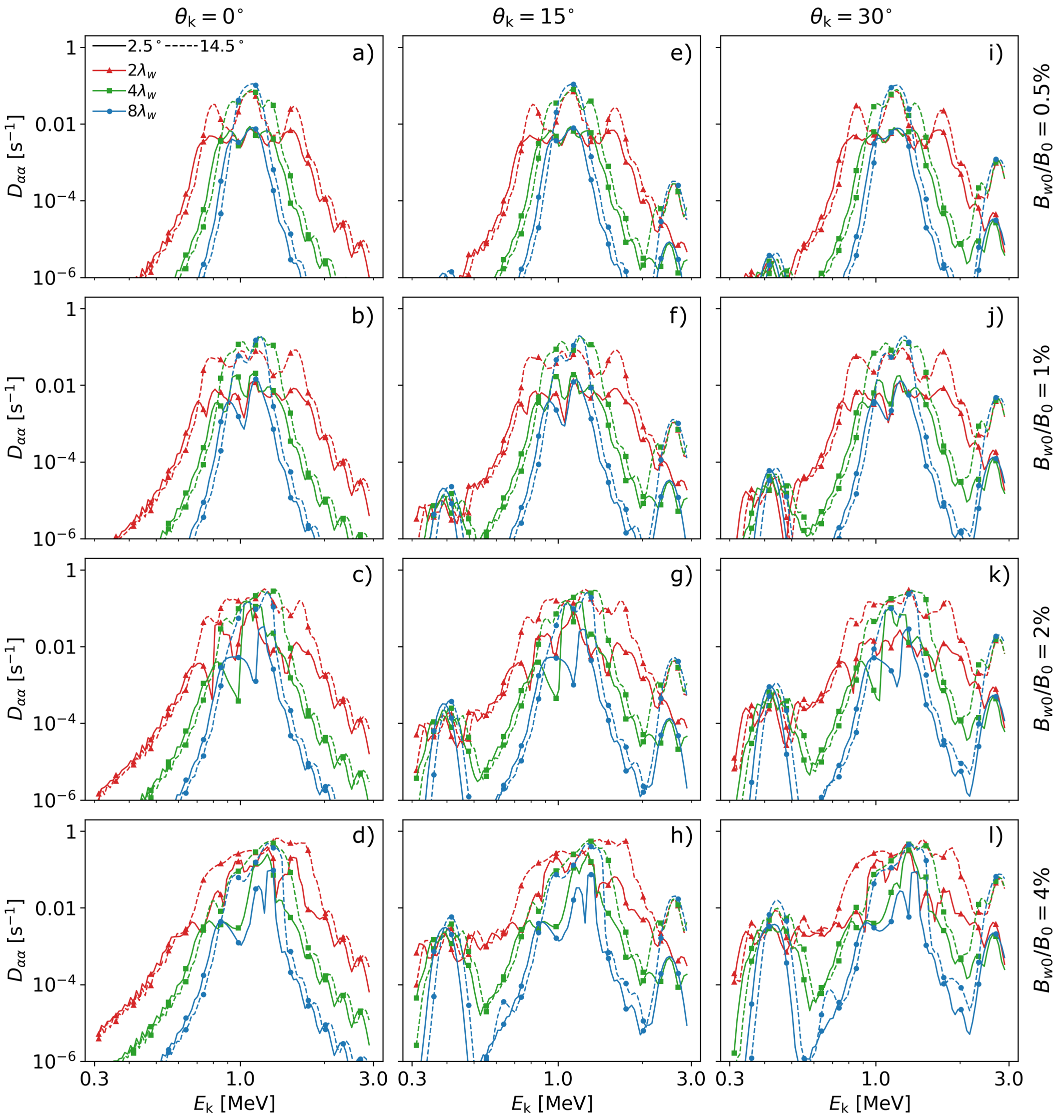

Figure 2. Pitch-angle diffusion coefficients calculated for various wave parameters. The solid and dashed lines represent $D_{\alpha\alpha}$ for pitch angles $\alpha_{\rm eq} = 2.5°$ and $\alpha_{\rm eq} = 14.5°$, respectively. Amplitude modulations of the wave packets are captured by different line colors and markers: red triangle for $d_{\rm e} = 2\lambda_{\rm w}$, green square for $d_{\rm e} = 4\lambda_{\rm w}$, and blue circle for $d_{\rm e} = 8\lambda_{\rm w}$. a-d) Diffusion coefficients for parallel-propagating waves, with amplitude increased by the factor of two in each row, going from $B_{\rm w0}/B_0 = 0.5\%$ to $B_{\rm w0}/B_0 = 4\%$. e-h) Diffusion coefficients for wave normal angle $\theta_{\rm k} = 15°$. i-l) Diffusion coefficients for wave normal angle $\theta_{\rm k} = 30°$.

to those caused by pure nonresonant scattering in the parallel-propagating case. A further increase of WNA to $\theta_{\mathrm{k}} = 30°$ enhances the peak nonlinear diffusion rate 2-3 times and shifts the minimum resonance energy to slightly higher values (Figures 2i-l). Due to the high absolute values of $D_{\alpha\alpha}$ near $E_{\mathrm{k}} = 450\,\mathrm{keV}$ in Figure 2l, the differences between $\alpha_{\mathrm{eq}} = 2.5°$ and $\alpha_{\mathrm{eq}} = 14.5°$ related to anomalous scattering start becoming apparent. Otherwise, the increase in WNA does not bring qualitative changes.

Using the backward-in-time simulation method outlined in Section 2.1, we obtained the PSD of particles pushed into the loss cone and then calculated precipitation ratios using Equation 3 with α_{sc90} value corresponding to the ELFIN spacecraft orbit (altitude of 450 km). The resulting precipitation ratios are shown in Figure 3. A comparison between nonresonant scattering by modulated waves in Figures 3a and 2a reveals that the precipitation profile near the fundamental resonance aligns more closely with the diffusion coefficients at higher pitch angles ($\alpha_{\mathrm{eq}} = 14.5°$) than those near the loss cone ($\alpha_{\mathrm{eq}} = 2.5°$). This suggests that precipitating particles predominantly originate at higher pitch angles. In the high-amplitude cases (Figures 3b-d), the diffusion coefficients near the fundamental resonance are always large enough ($D_{\alpha\alpha} > 0.01\,\mathrm{s}^{-1}$) to completely fill the loss cone (precipitation ratios close to 1). As expected, strong nonresonant scattering extends the energy range in which the loss cone is full and can cause nonnegligible precipitation down to about 400 keV.

The precipitation caused by nonlinear sub-cyclotron resonance is significant only when the amplitude rises above 1%, as demonstrated in Figures 3e-h. In agreement with the diffusion coefficient calculation, the interplay of nonresonant and nonlinear resonances yields a flat precipitation profile. Increase of WNA from 15° to 30° further enhances the precipitation, reaching a ratio of ~ 1 in Figure 3l. Further increase in obliquity to 45° has only minor effect on the resulting precipitation and is therefore not plotted here.

The numerical prediction of precipitation ratios can be compared to electron flux observations provided by the ELFIN spacecraft. Figure 4a shows the EMIC-driven electron precipitation event of March 31, 2021, detected by the ELFIN-A spacecraft in the northern hemisphere. Precipitation ratios close to one were detected at energies near 1 MeV, with nonnegligible values (> 0.1) reaching down to about 200 keV. In the time interval of presumed EMIC activity (dashed magenta lines), the trapped electron flux in Figure 4b steadily decreases with energy. Note that we remove low-count data by requir-

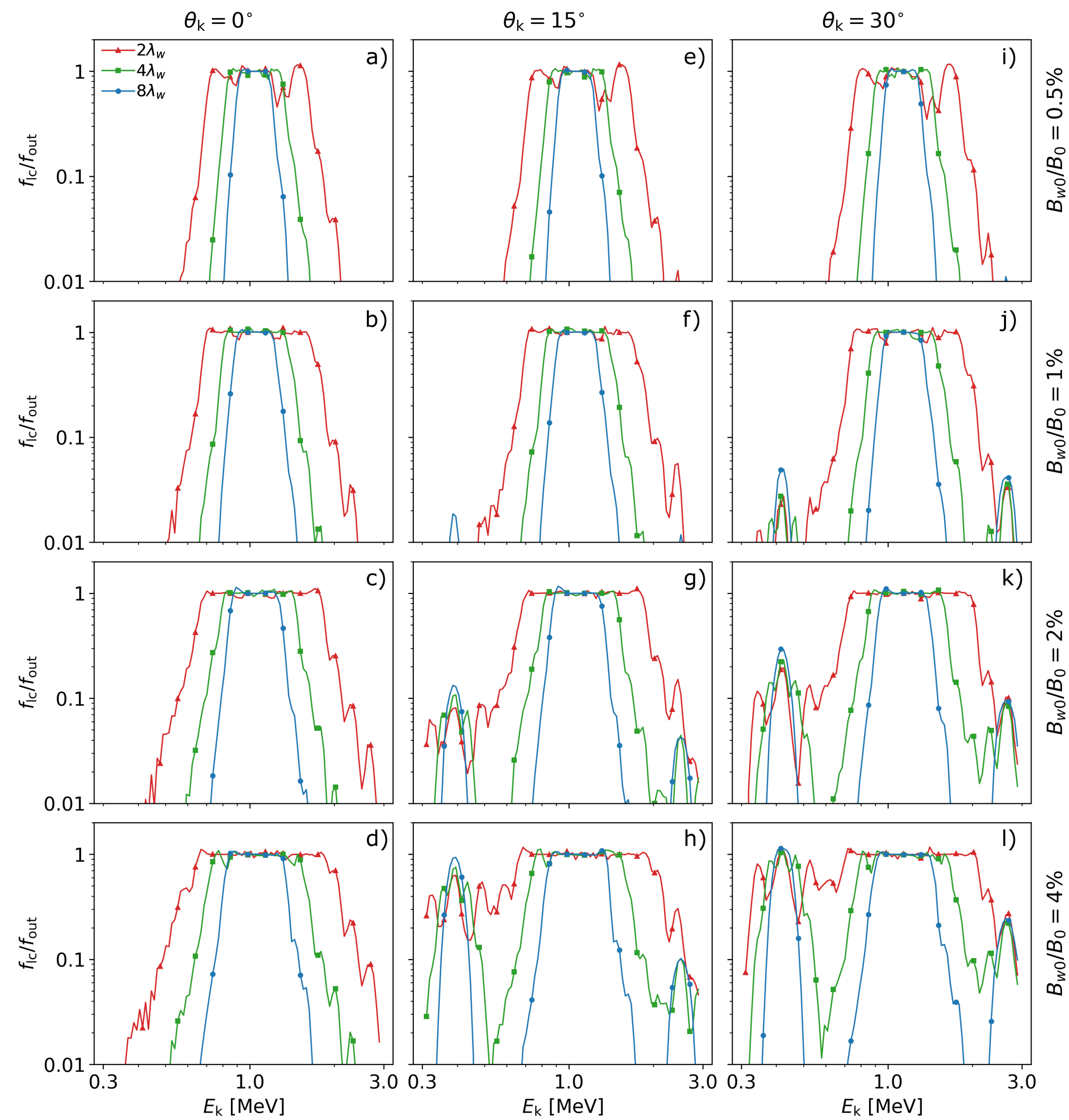

Figure 3. Electron precipitation ratios for various wave parameters. The panel layout and line colors are the same as in Figure 2.

ing a maximum percentage error of 50%. The detailed plots of precipitation ratios during each half-spin in Figure 4c display a large variability, but a main peak around 1 MeV and a secondary peak close to 400 keV can be discerned.

Figure 4d displays averaged precipitation ratios from six selected events (details in Section 2.2 and Table S1 in the Supporting Information). We recall that $E_{\mathrm{k}}/E_{\mathrm{k}}^{*} = 1$ is the lowest energy bin with a high precipitation ratio > 0.75. Simulation results in Figure 3 show that the minimum resonance energy E_{Rmin} is typically slightly higher than E_{k}^{*}. On the other hand, the $n = 1/2$ resonance does not appear at $E_{\mathrm{Rmin}}/2$ but instead somewhere between $0.3E_{\mathrm{Rmin}}$ and $0.4E_{\mathrm{Rmin}}$ (for E_{Rmin} near 1 MeV). Hence, the secondary peak or plateau from the fractional resonance should appear roughly in the $E_{\mathrm{k}}/E_{\mathrm{k}}^{*} = 0.3$ to 0.7 range (highlighted in blue). The enhanced precipitation near $E_{\mathrm{k}}/E_{\mathrm{k}}^{*} = 0.5$ greatly differs from the steep decrease of precipitation ratio predicted by nonresonant scattering (Figures 3a-d). These observations can be explained either by a low-power EMIC wave component with extremely low E_{Rmin}, or by the nonlinear sub-cyclotron scattering, or their combination.

We must point out that according to the simulation with extremely large wave amplitudes and short subpackets (Figures 3h,l), the criterion $f_{\mathrm{in}}/f_{\mathrm{out}} > 0.75$ could be met by the sub-cyclotron resonance peak. However, the observations show ratios as large as $f_{\mathrm{in}}/f_{\mathrm{out}} > 1$ in the $E_{\mathrm{k}}/E_{\mathrm{k}}^{*} > 1$ range, which goes even above the simulated extreme case. Moreover, since the selection process behind the (Capannolo et al., 2023a) dataset aimed to exclude contributions from whistler-mode waves (see Section 2.2), we would have no explanation for the significant $f_{\mathrm{in}}/f_{\mathrm{out}}$ values below E_{k}^{*}. The faint $n = 1/3$ resonance in Figure 1f is too weak for substantial precipitation. Thus, it is safe to assume that the peak above E_{k}^{*} originates in the fundamental resonance.

4 Discussion and Conclusion

We have demonstrated that the nonlinear sub-cyclotron scattering can contribute to EMIC-driven electron precipitation in the energy range of hundreds of keV. Precipitation ratios remain low unless wave amplitudes exceed $0.01B_0$, explaining the scarcity of ELFIN-detected events with clear nonlinear patterns. Despite these low ratios, the precipitating flux can be substantial. Taking the ELFIN-A measurements of trapped electron flux from Figure 4b, the values at $E_{\mathrm{k1}} = 300$ keV are ten times larger than at $E_{\mathrm{k2}} =$

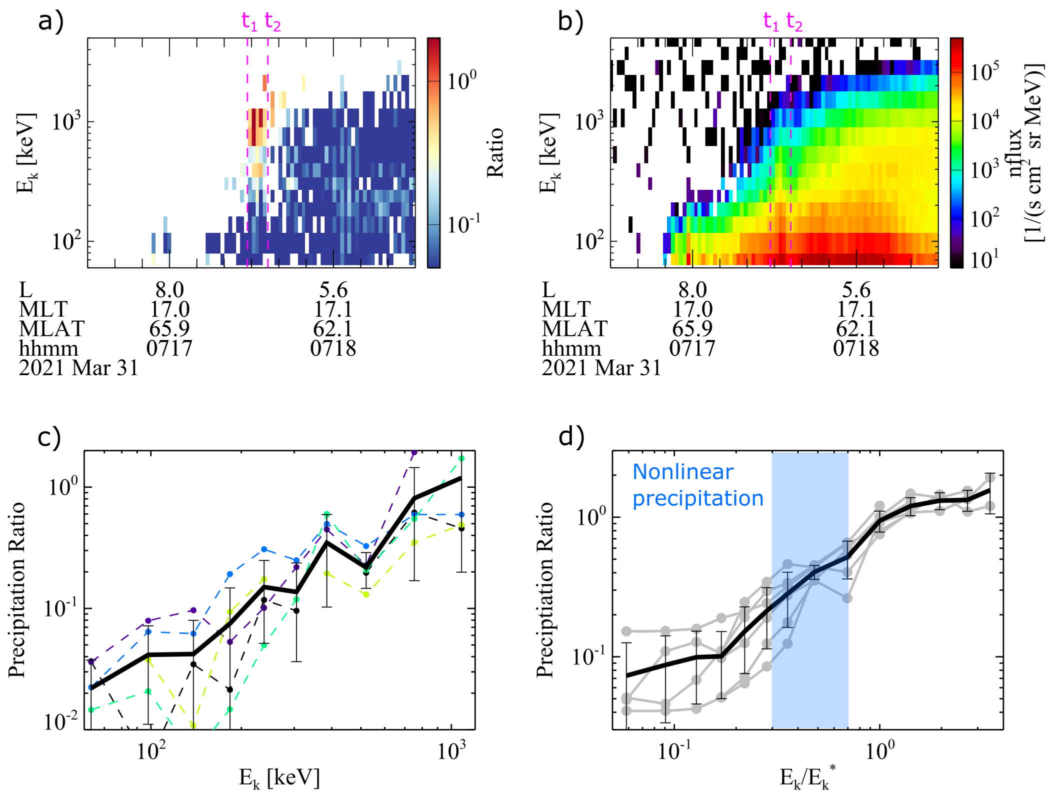

Figure 4. Electron precipitation detected by the ELFIN CubeSats. a) Precipitation ratios detected by ELFIN-A on March 31, 2021 in the northern hemisphere, with a typical EMIC-driven precipitation pattern shown between $t_1 = $ 07:17:30 and $t_2 = $ 07:17:33 (dashed magenta lines). b) Trapped electron number flux. c) Line plots of precipitation ratios between t_1 and t_2, with each dashed colored line representing a single half-spin and the thick black line showing the average with standard deviations as errorbars. d) Statistical precipitation ratios in selected events plotted against normalized energy (see Section 2.2 for the definition of E_k^* and event selection). Grey lines represent averages over individual events, the black line is the sample average with errorbars showing the standard deviations. The light blue area highlights the energy range where the strongest effects from the $n = 1/2$ nonlinear resonance are expected.

1 MeV. A precipitation ratio of 0.1 at E_{k1} then yields a comparable precipitating flux to a ratio of 1.0 at E_{k2}. This observation aligns with the predominance of precipitating flux peaks at energies $E_k < 1$, MeV in the dataset of Hendry et al. (2017).

Our numerical predictions are largely insensitive to variations in the initial pitch-angle distribution, which we confirmed by recalculating results in Figure 3 using an isotropic initial PSD ($U_{t\perp} = U_{t\|}$). Our choice of wave model is supported only by case studies as those of Nakamura et al. (2015) and Ojha et al. (2021), since a statistical analysis of amplitude modulations in near-equatorial EMIC waves is not available in published literature. An alternate model with a $16\lambda_w$ long subpacket with sharp edges results in suppression of nonresonant spreading of the $n = 1/2$ precipitation peak, but the overall picture remains the same. And while interactions with wave packets extending to higher latitudes might broaden resonance peaks towards higher energies, obtaining realistic results would require considering the latitude-dependent evolution of B_w and θ_k. To address these complexities, we plan to construct improved EMIC wave models for future investigations.

In summary, our simulations reveal that nonlinear sub-cyclotron resonance of electrons with quasiparallel EMIC waves substantially amplifies precipitation fluxes at energies below the minimum resonance energy. Together with nonresonant scattering, these two effects can be used to explain the enhanced precipitation ratios observed by ELFIN in the sub-MeV part of the energy spectrum. To conclusively confirm the importance of these two scattering processes in energetic electron precipitation, a dataset of conjugate measurements between equatorial radiation belt probes and LEO spacecraft is needed. We hope that such data will become more abundant in the future thanks to the emergence of low-cost CubeSat missions.

Open Research Section

Processed data from the test-particle simulations and the list of precipitation events from Capannolo et al. (2023a) are publicly available (Hanzelka, Li, Qin, et al., 2023; Capannolo et al., 2023b). The ELFIN data (The ELFIN CubeSat Mission Team, 2023) were processed using SPEDAS routines specifically written for processing ELFIN data by the ELFIN UCLA team. The SPEDAS library is described in Angelopoulos et al. (2019).

Acknowledgments

The research at Boston University is supported by NASA grants 80NSSC20K0698, 80NSSC20K1270, and 80NSSC21K1312, as well as the NSF grant AGS-2019950. QM would like to acknowledge the NASA grant 80NSSC20K0196 and the NSF grant AGS-2225445. LG gratefully acknowledges the NASA FINESST grant 80NSSC20K1506. All authors acknowledge the efforts by Geospace Environment Modeling focus group "Self-Consistent Inner Magnetospheric Modeling".

References

Albert, J. M., & Bortnik, J. (2009, June). Nonlinear interaction of radiation belt electrons with electromagnetic ion cyclotron waves. *Geophys. Res. Lett.*, *36*(12), L12110. doi: 10.1029/2009GL038904

Allen, R. C., Zhang, J. C., Kistler, L. M., Spence, H. E., Lin, R. L., Klecker, B., … Jordanova, V. K. (2015, July). A statistical study of EMIC waves observed by Cluster: 1. Wave properties. *J. Geophys. Res. Space Physics*, *120*(7), 5574-5592. doi: 10.1002/2015JA021333

An, X., Artemyev, A., Angelopoulos, V., Zhang, X., Mourenas, D., & Bortnik, J. (2022, September). Nonresonant Scattering of Relativistic Electrons by Electromagnetic Ion Cyclotron Waves in Earth's Radiation Belts. *Phys. Rev. Lett.*, *129*(13), 135101. doi: 10.1103/PhysRevLett.129.135101

Angelopoulos, V., Cruce, P., Drozdov, A., Grimes, E. W., Hatzigeorgiu, N., King, D. A., … Schroeder, P. (2019, January). The Space Physics Environment Data Analysis System (SPEDAS). *Space Sci. Rev.*, *215*(1), 9. doi: 10.1007/s11214-018-0576-4

Angelopoulos, V., Tsai, E., Bingley, L., Shaffer, C., Turner, D. L., Runov, A., … Zhang, G. Y. (2020, July). The ELFIN Mission. *Space Sci. Rev.*, *216*(5), 103. doi: 10.1007/s11214-020-00721-7

Angelopoulos, V., Zhang, X. J., Artemyev, A. V., Mourenas, D., Tsai, E., Wilkins, C., … Zarifian, A. (2023, August). Energetic Electron Precipitation Driven by Electromagnetic Ion Cyclotron Waves from ELFIN's Low Altitude Perspective. *Space Sci. Rev.*, *219*(5), 37. doi: 10.1007/s11214-023-00984-w

Baker, D. N., Hoxie, V., Zhao, H., Jaynes, A. N., Kanekal, S., Li, X., & Elkington, S. (2019, April). Multiyear Measurements of Radiation Belt Electrons:

Acceleration, Transport, and Loss. *J. Geophys. Res. Space Physics*, *124*(4), 2588-2602. doi: 10.1029/2018JA026259

Bortnik, J., Albert, J. M., Artemyev, A., Li, W., Jun, C.-W., Grach, V. S., & Demekhov, A. G. (2022, June). Amplitude Dependence of Nonlinear Precipitation Blocking of Relativistic Electrons by Large Amplitude EMIC Waves. *Geophys. Res. Lett.*, *49*(12), e98365. doi: 10.1029/2022GL098365

Capannolo, L., Li, W., Ma, Q., Qin, M., Shen, X.-C., Angelopoulos, V., ... Hanzelka, M. (2023a, October). Electron Precipitation Observed by ELFIN Using Proton Precipitation as a Proxy for Electromagnetic Ion Cyclotron (EMIC) Waves. *Geophys. Res. Lett.*, *50*(21), e2023GL103519. doi: 10.1029/2023GL103519

Capannolo, L., Li, W., Ma, Q., Qin, M., Shen, X.-C., Angelopoulos, V., ... Hanzelka, M. (2023b, March). EMIC-driven precipitation events observed by ELFIN, using proton precipitation as a proxy for EMIC waves [Dataset]. *Zenodo*. doi: 10.5281/zenodo.7697272

Capannolo, L., Li, W., Spence, H., Johnson, A. T., Shumko, M., Sample, J., & Klumpar, D. (2021, March). Energetic Electron Precipitation Observed by FIREBIRD II Potentially Driven by EMIC Waves: Location, Extent, and Energy Range From a Multievent Analysis. *Geophys. Res. Lett.*, *48*(5), e91564. doi: 10.1029/2020GL091564

Chen, L., Thorne, R. M., Bortnik, J., & Zhang, X.-J. (2016, October). Nonresonant interactions of electromagnetic ion cyclotron waves with relativistic electrons. *J. Geophys. Res. Space Physics*, *121*(10), 9913-9925. doi: 10.1002/2016JA022813

Chen, L., Zhu, H., & Zhang, X. (2019, June). Wavenumber Analysis of EMIC Waves. *Geophys. Res. Lett.*, *46*(11), 5689-5697. doi: 10.1029/2019GL082686

Clilverd, M. A., Duthie, R., Hardman, R., Hendry, A. T., Rodger, C. J., Raita, T., ... Milling, D. K. (2015, May). Electron precipitation from EMIC waves: A case study from 31 May 2013. *J. Geophys. Res. Space Physics*, *120*(5), 3618-3631. doi: 10.1002/2015JA021090

Denton, R. E., Ofman, L., Shprits, Y. Y., Bortnik, J., Millan, R. M., Rodger, C. J., ... Komar, C. (2019, July). Pitch Angle Scattering of Sub-MeV Relativistic Electrons by Electromagnetic Ion Cyclotron Waves. *J. Geophys. Res. Space*

Physics, *124* (7), 5610-5626. doi: 10.1029/2018JA026384

Engebretson, M. J., Posch, J. L., Wygant, J. R., Kletzing, C. A., Lessard, M. R., Huang, C. L., ... Shiokawa, K. (2015, July). Van Allen probes, NOAA, GOES, and ground observations of an intense EMIC wave event extending over 12 h in magnetic local time. *J. Geophys. Res. Space Physics*, *120* (7), 5465-5488. doi: 10.1002/2015JA021227

Fu, X., Guo, Z., Dong, C., & Gary, S. P. (2015, May). Nonlinear subcyclotron resonance as a formation mechanism for gaps in banded chorus. *Geophys. Res. Lett.*, *42* (9), 3150-3159. doi: 10.1002/2015GL064182

Hanzelka, M., Li, W., & Ma, Q. (2023, April). Parametric analysis of pitch angle scattering and losses of relativistic electrons by oblique EMIC waves. *Frontiers in Astronomy and Space Sciences*, *10*, 1163515. doi: 10.3389/fspas.2023.1163515

Hanzelka, M., Li, W., Qin, M., Capannolo, L., Shen, X., Ma, Q., ... Angelopoulos, V. (2023, October). Sub-MeV electron precipitation driven by EMIC waves through nonlinear sub-cyclotron resonances: Processed test-particle data [Dataset]. *Figshare*. doi: 10.6084/m9.figshare.23960964

Hendry, A. T., Rodger, C. J., & Clilverd, M. A. (2017, February). Evidence of sub-MeV EMIC-driven electron precipitation. *Geophys. Res. Lett.*, *44* (3), 1210-1218. doi: 10.1002/2016GL071807

Hendry, A. T., Santolik, O., Kletzing, C. A., Rodger, C. J., Shiokawa, K., & Baishev, D. (2019, July). Multi-instrument Observation of Nonlinear EMIC-Driven Electron Precipitation at sub-MeV Energies. *Geophys. Res. Lett.*, *46* (13), 7248-7257. doi: 10.1029/2019GL082401

Horne, R. B., & Thorne, R. M. (1998, August). Potential waves for relativistic electron scattering and stochastic acceleration during magnetic storms. *Geophys. Res. Lett.*, *25* (15), 3011-3014. doi: 10.1029/98GL01002

Jordanova, V. K., Farrugia, C. J., Thorne, R. M., Khazanov, G. V., Reeves, G. D., & Thomsen, M. F. (2001, January). Modeling ring current proton precipitation by electromagnetic ion cyclotron waves during the May 14-16, 1997, storm. *J. Geophys. Res.*, *106* (A1), 7-22. doi: 10.1029/2000JA002008

Li, W., & Hudson, M. K. (2019, November). Earth's Van Allen Radiation Belts: From Discovery to the Van Allen Probes Era. *J. Geophys. Res. Space Physics*, *124*(11), 8319-8351. doi: 10.1029/2018JA025940

Li, W., Shprits, Y. Y., & Thorne, R. M. (2007, October). Dynamic evolution of energetic outer zone electrons due to wave-particle interactions during storms. *J. Geophys. Res. Space Physics*, *112*(A10), A10220. doi: 10.1029/2007JA012368

Lyu, X., Ma, Q., Tu, W., Li, W., & Capannolo, L. (2022, October). Modeling the Simultaneous Dropout of Energetic Electrons and Protons by EMIC Wave Scattering. *Geophys. Res. Lett.*, *49*(20), e2022GL101041. doi: 10.1029/2022GL101041

Ma, Q., Li, W., Thorne, R. M., Nishimura, Y., Zhang, X. J., Reeves, G. D., … Angelopoulos, V. (2016, May). Simulation of energy-dependent electron diffusion processes in the Earth's outer radiation belt. *J. Geophys. Res. Space Physics*, *121*(5), 4217-4231. doi: 10.1002/2016JA022507

Meredith, N. P., Horne, R. B., Kersten, T., Fraser, B. J., & Grew, R. S. (2014, July). Global morphology and spectral properties of EMIC waves derived from CRRES observations. *J. Geophys. Res. Space Physics*, *119*(7), 5328-5342. doi: 10.1002/2014JA020064

Min, K., Kim, J., Ma, Q., Jun, C.-W., & Liu, K. (2022, January). Unusual high frequency EMIC waves: Detailed analysis of EMIC wave excitation and energy coupling between EMIC and magnetosonic waves. *Advances in Space Research*, *69*(1), 35-47. doi: 10.1016/j.asr.2021.07.039

Min, K., Lee, J., Keika, K., & Li, W. (2012, May). Global distribution of EMIC waves derived from THEMIS observations. *J. Geophys. Res. Space Physics*, *117*(A5), A05219. doi: 10.1029/2012JA017515

Miyoshi, Y., Sakaguchi, K., Shiokawa, K., Evans, D., Albert, J., Connors, M., & Jordanova, V. (2008, December). Precipitation of radiation belt electrons by EMIC waves, observed from ground and space. *Geophys. Res. Lett.*, *35*(23), L23101. doi: 10.1029/2008GL035727

Nakamura, S., Omura, Y., Shoji, M., Nosé, M., Summers, D., & Angelopoulos, V. (2015, September). Subpacket structures in EMIC rising tone emissions observed by the THEMIS probes. *J. Geophys. Res. Space Physics*, *120*(9), 7318-7330. doi: 10.1002/2014JA020764

Ojha, B., Omura, Y., Singh, S., & Lakhina, G. S. (2021, November). Multipoint Analysis of Source Regions of EMIC Waves and Rapid Growth of Subpackets.

J. Geophys. Res. Space Physics, *126*(11), e29514. doi: 10.1029/2021JA029514

Reeves, G. D., Spence, H. E., Henderson, M. G., Morley, S. K., Friedel, R. H. W., Funsten, H. O., ... Niehof, J. T. (2013, August). Electron Acceleration in the Heart of the Van Allen Radiation Belts. *Science*, *341*(6149), 991-994. doi: 10.1126/science.1237743

Saikin, A. A., Zhang, J. C., Smith, C. W., Spence, H. E., Torbert, R. B., & Kletzing, C. A. (2016, May). The dependence on geomagnetic conditions and solar wind dynamic pressure of the spatial distributions of EMIC waves observed by the Van Allen Probes. *J. Geophys. Res. Space Physics*, *121*(5), 4362-4377. doi: 10.1002/2016JA022523

Seppälä, A., Clilverd, M. A., Beharrell, M. J., Rodger, C. J., Verronen, P. T., Andersson, M. E., & Newnham, D. A. (2015, October). Substorm-induced energetic electron precipitation: Impact on atmospheric chemistry. *Geophys. Res. Lett.*, *42*(19), 8172-8176. doi: 10.1002/2015GL065523

Shprits, Y. Y., Subbotin, D. A., Meredith, N. P., & Elkington, S. R. (2008, November). Review of modeling of losses and sources of relativistic electrons in the outer radiation belt II: Local acceleration and loss. *J. Atmos. Sol.-Terr. Phys.*, *70*(14), 1694-1713. doi: 10.1016/j.jastp.2008.06.014

Summers, D., Thorne, R. M., & Xiao, F. (1998, September). Relativistic theory of wave-particle resonant diffusion with application to electron acceleration in the magnetosphere. *J. Geophys. Res.*, *103*(A9), 20487-20500. doi: 10.1029/98JA01740

The ELFIN CubeSat Mission Team. (2023). *Electron Losses and Field Investigation: Home Page.* `https://data.elfin.ucla.edu`. (Accessed: 2023-11-01)

Thorne, R. M. (1977, January). Energetic radiation belt electron precipitation: a natural depletion mechanism for stratospheric ozone. *Science*, *195*, 287-289. doi: 10.1126/science.195.4275.287

Ukhorskiy, A. Y., Shprits, Y. Y., Anderson, B. J., Takahashi, K., & Thorne, R. M. (2010, May). Rapid scattering of radiation belt electrons by storm-time EMIC waves. *Geophys. Res. Lett.*, *37*(9), L09101. doi: 10.1029/2010GL042906

Usanova, M. E., Drozdov, A., Orlova, K., Mann, I. R., Shprits, Y., Robertson, M. T., ... Wygant, J. (2014, March). Effect of EMIC waves on relativistic and ultrarelativistic electron populations: Ground-based and Van

Allen Probes observations. *Geophys. Res. Lett.*, *41*(5), 1375-1381. doi: 10.1002/2013GL059024

Wang, G., Su, Z., Zheng, H., Wang, Y., Zhang, M., & Wang, S. (2017, February). Nonlinear fundamental and harmonic cyclotron resonant scattering of radiation belt ultrarelativistic electrons by oblique monochromatic EMIC waves. *J. Geophys. Res. Space Physics*, *122*(2), 1928-1945. doi: 10.1002/2016JA023451

Zenitani, S., & Umeda, T. (2018, November). On the Boris solver in particle-in-cell simulation. *Phys. Plasmas*, *25*(11), 112110. doi: 10.1063/1.5051077

Zhang, X. J., Li, W., Thorne, R. M., Angelopoulos, V., Bortnik, J., Kletzing, C. A., ... Hospodarsky, G. B. (2016, December). Statistical distribution of EMIC wave spectra: Observations from Van Allen Probes. *Geophys. Res. Lett.*, *43*(24), 12,348-12,355. doi: 10.1002/2016GL071158

Zhu, H., Chen, L., Claudepierre, S. G., & Zheng, L. (2020, February). Direct Evidence of the Pitch Angle Scattering of Relativistic Electrons Induced by EMIC Waves. *Geophys. Res. Lett.*, *47*(4), e85637. doi: 10.1029/2019GL085637

Figure 1.

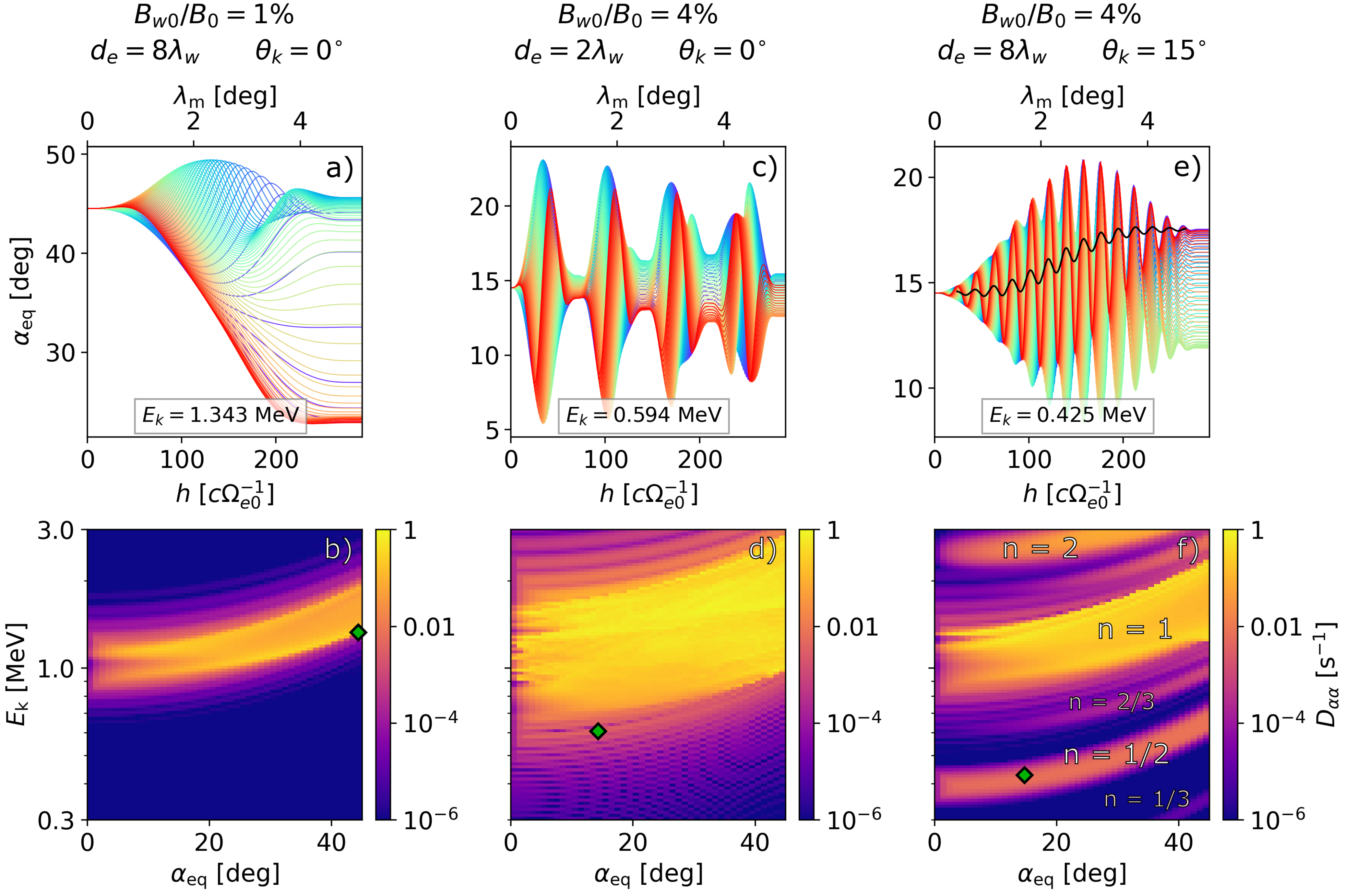

$B_{w0}/B_0 = 1\%$
$d_e = 8\lambda_w \quad \theta_k = 0^\circ$
$B_{w0}/B_0 = 4\%$
$d_e = 2\lambda_w \quad \theta_k = 0^\circ$
$B_{w0}/B_0 = 4\%$
$d_e = 8\lambda_w \quad \theta_k = 15^\circ$
$\lambda_{\rm m}$ [deg]
a)
c)
e)
$\alpha_{\rm eq}$ [deg]
$E_k = 1.343$ MeV
$E_k = 0.594$ MeV
$E_k = 0.425$ MeV
h [$c\Omega_{e0}^{-1}$]
b)
d)
f)
$E_{\rm k}$ [MeV]
n = 2
n = 1
n = 2/3
n = 1/2
n = 1/3
$D_{\alpha\alpha}$ [s^{-1}]

Figure 2.

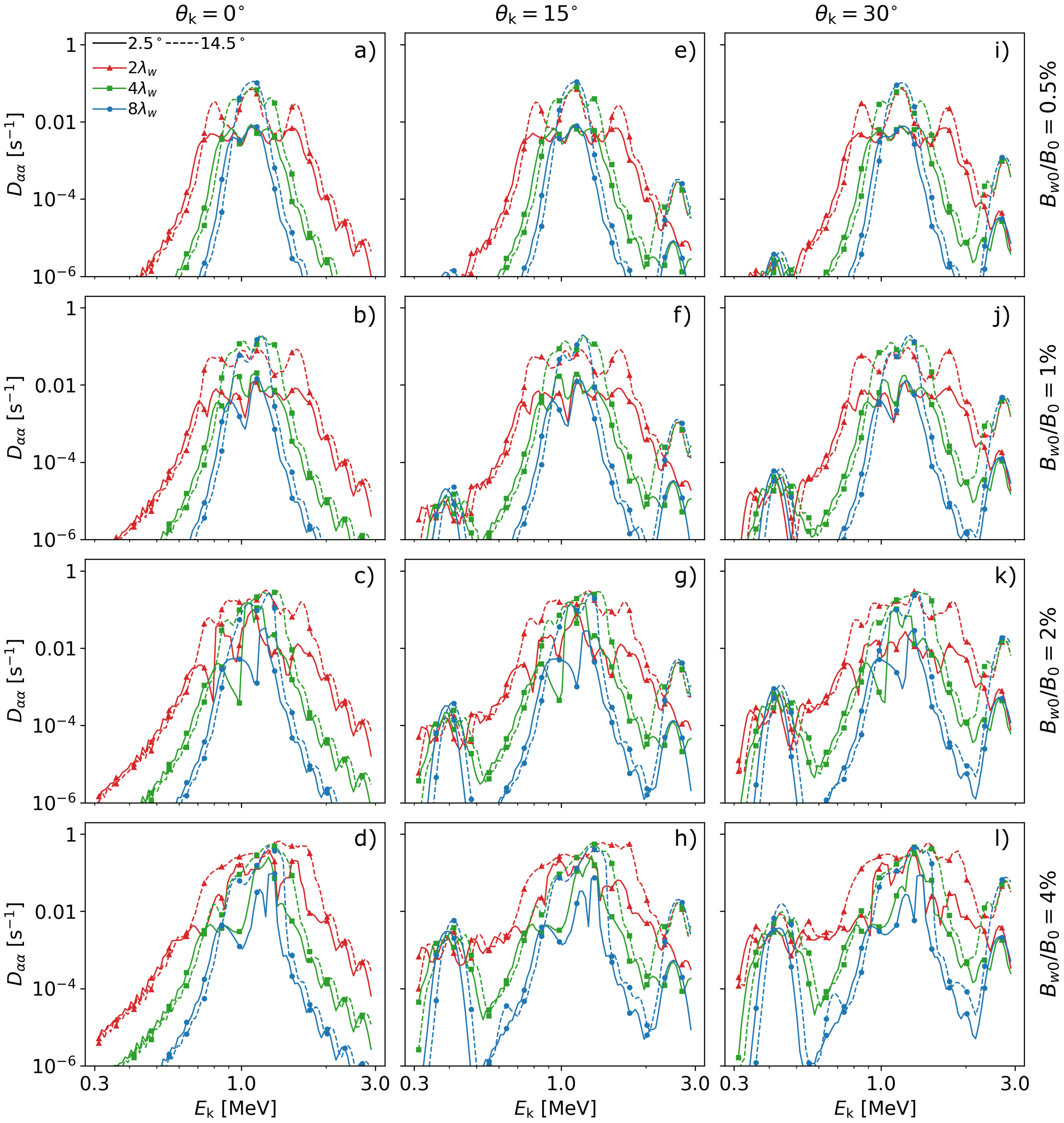

$\theta_k = 0^\circ$
$\theta_k = 15^\circ$
$\theta_k = 30^\circ$
2.5° 14.5°
$2\lambda_w$
$4\lambda_w$
$8\lambda_w$
a)
b)
c)
d)
e)
f)
g)
h)
i)
j)
k)
l)
$D_{\alpha\alpha}$ [s^{-1}]
$B_{w0}/B_0 = 0.5\%$
$B_{w0}/B_0 = 1\%$
$B_{w0}/B_0 = 2\%$
$B_{w0}/B_0 = 4\%$
E_k [MeV]
1
0.01
10^{-4}
10^{-6}
0.3
1.0
3.0

Figure 3.

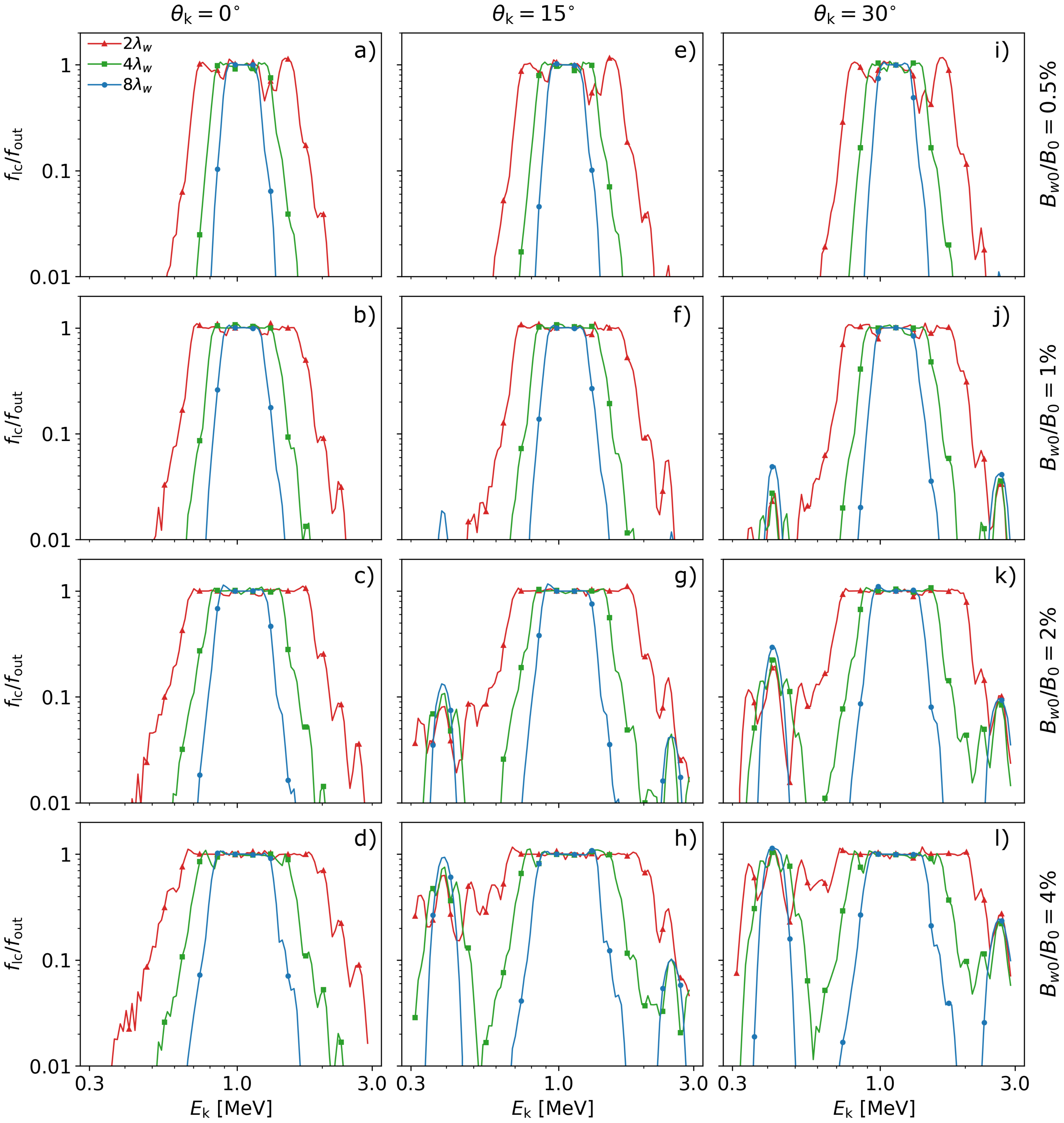

$\theta_k = 0^\circ$
$\theta_k = 15^\circ$
$\theta_k = 30^\circ$
$2\lambda_w$
$4\lambda_w$
$8\lambda_w$
a)
b)
c)
d)
e)
f)
g)
h)
i)
j)
k)
l)
$B_{w0}/B_0 = 0.5\%$
$B_{w0}/B_0 = 1\%$
$B_{w0}/B_0 = 2\%$
$B_{w0}/B_0 = 4\%$
f_{lc}/f_{out}
E_k [MeV]
0.01
0.1
1
0.3
1.0
3.0

Figure 4.

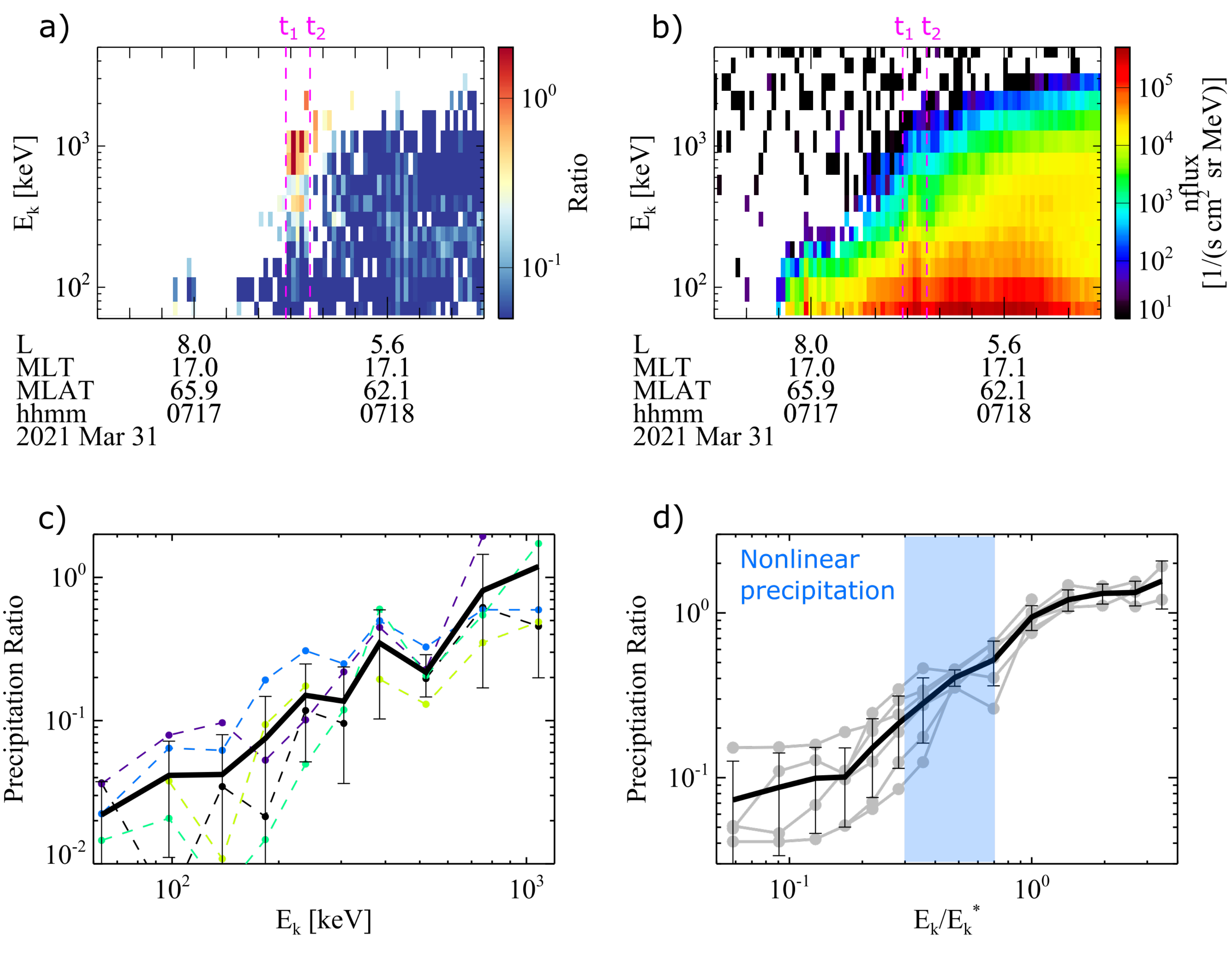

a)
t1 t2
Ek [keV]
Ratio
L 8.0 5.6
MLT 17.0 17.1
MLAT 65.9 62.1
hhmm 0717 0718
2021 Mar 31
b)
t1 t2
Ek [keV]
nflux [1/(s cm2 sr MeV)]
L 8.0 5.6
MLT 17.0 17.1
MLAT 65.9 62.1
hhmm 0717 0718
2021 Mar 31
c)
Precipitation Ratio
Ek [keV]
d)
Nonlinear precipitation
Precipitation Ratio
Ek/Ek*